Axisymmetric form of the material point method with applications to upsetting and Taylor impact problems

Deborah Sulsky[a],[*], Howard L. Schreyer[b]

[a]*Department of Mathematics and Statistics, University of New Mexico, Albuquerque, NM 87131, USA*
[b]*Department of Mechanical Engineering, University of New Mexico, Albuquerque, NM 87131, USA*

Abstract

The material point method is an evolution of particle-in-cell methods which utilize two meshes, one a material or Lagrangian mesh defined over material of the body under consideration, and the second a spatial or Eulerian mesh defined over the computational domain. Although meshes are used, they have none of the negative aspects normally associated with conventional Eulerian or Lagrangian approaches. The advantages of both the Eulerian and Lagrangian methods are achieved by using the appropriate frame for each aspect of the computation, with a mapping between the two meshes that is performed at each step in the loading process. The numerical dissipation normally displayed by an Eulerian method because of advection is avoided by using a Lagrangian step; the mesh distortion associated with the Lagrangian method is prevented by mapping to a user-controlled mesh. Furthermore, explicit material points can be tracked through the process of deformation, thereby alleviating the need to map history variables. As a consequence, problems which have caused severe numerical difficulties with conventional methods are handled fairly routinely. Examples of such problems are the upsetting of billets and the Taylor problem of cylinders impacting a rigid wall. Numerical solutions to these problems are obtained with the material point method and where possible comparisons with experimental data and existing numerical solutions are presented.

1. Introduction

The material point method evolved from a particle-in-cell (PIC) method called FLIP, developed at Los Alamos National Laboratory [1,2], to a new method capable of handling material strength and stiffness [3,4]. PIC methods utilize two meshes, one a material or Lagrangian mesh defined over material of the body under consideration, and the second a spatial or Eulerian mesh defined over the computational domain. The advantages of both the Eulerian and Lagrangian methods are achieved by using the appropriate frame for each aspect of the computation, with a mapping between the two meshes that is performed at each step in the loading process. The numerical dissipation due to advection normally associated with an Eulerian method is avoided by using a Lagrangian step; the mesh distortion associated with the Lagrangian method is prevented by mapping to a user-controlled mesh. Furthermore, explicit material points can be tracked throughout the deformation process, thereby eliminating the need to map history variables. As a consequence, problems which have caused numerical difficulties with conventional methods have been handled fairly routinely. In Section 3, two such examples will be considered, the upsetting of a cylindrical billet and the Taylor problem of a cylindrical rod impacting a rigid surface. Each of these simulations can be carried out without the difficulties usually associated with classical finite element methods such as remeshing and lock-up.

---

* Corresponding author.

The first implementations of the material point method were in one and two dimensions. This choice was not due to a theoretical limitation of the method, but merely represented the desire to have a simple testbed for the numerical algorithm. There also are many interesting problems for which the assumption of plane strain or plane stress is valid. The references [3,4] provide details of the formulation and discrete equations. In Section 2, the formulation is reviewed and augmented to show how the method can take advantage of azimuthal symmetry. The extension from two dimensions to three-dimensional axisymmetric problems is straightforward, and is an inexpensive way to extend the capability of the method to three-dimensional problems with the appropriate symmetry. A simulation in Section 3 of the elastic vibrations of a sphere provides validation of the axisymmetric form. The normal modes of vibration are known analytically and compare well with the numerically predicted results. Some numerical dissipation is present in the method because we use a lumped mass matrix [5]. This numerical simulation also quantifies the amount of numerical dissipation.

In the past, we have restricted our attention to isothermal problems. Now, an energy equation is also solved so that thermal effects can be included in the constitutive equations. This equation is also presented in Section 2 along with its discretization. In Section 3 a Johnson–Cook model for copper is implemented and tested in the Taylor problem against other published numerical solutions and experimental findings. The Johnson–Cook model includes strain hardening, rate effects and thermal softening. Also, in Section 3 results from a simulation of the upsetting of a cylindrical billet are reported and compared with similar numerical simulations in the literature.

2. Governing equations

In the material point method, a set of material points is tracked throughout the deformation history of a body. The full numerical solution is calculated at these points; so, for example these points have mass, displacement, velocity, stress, strain, plastic strain, internal energy and temperature associated with them. The initial values of these quantities are set from initial data given in the problem of interest and subsequent values are obtained by computing the interaction between these points consistent with conservation of mass, momentum and energy. To compute the interaction, the information carried by the material points is projected onto a background finite element mesh where equations of motion are solved in an updated Lagrangian frame. Information from this solution is then used to update the material points. This solution on the mesh is called the Lagrangian phase of the calculation. Once the material points have been updated, the mesh can be discarded and a new mesh used in subsequent time steps. This allows the mesh to be chosen by the user, for example, to resolve sharp gradients. In our computations we have chosen a regular rectangular mesh each time step; this choice avoids difficulties with mesh tangling. Since the mesh is discarded, the current solution on a new mesh must be determined from the data carried by the material points. The movement of the mesh relative to the material points models convection, and is called the convective phase of the calculation. In this section, we describe the role of the material points and finite element mesh in the solution of the mass, momentum and energy equations.

2.1. Conservation of mass

A solid body under investigation occupies a region $\Omega_3(0) \subseteq R^3$ initially and $\Omega_3(t) \subseteq R^3$ for time $t > 0$. To be compatible with the assumption of axisymmetry, the geometry of the region under study, $\Omega_3(t)$, must be a solid of revolution constructed by rotating a two-dimensional cross-section, $\Omega_2(t) \subseteq R^2$, about the symmetry axis. Consider a cylindrical coordinate system with coordinates (r, θ, z), and with z along the axis of symmetry. Points in $\Omega_2(t)$ have a constant value of θ and therefore can be specified by giving their (r, z) coordinates. If a material point is identified at position $X = (R, Z)$ initially then its current position $x = (r, z)$ at time $t > 0$ is a function of X and t with $x(X, 0) = X$. It is assumed that this function is invertible so that we may also consider X to be a function of x and t.

Divide the initial configuration $\Omega_2(0)$ into N_p disjoint subdomains with $\Omega_2 = \cup_{p=1}^{N_p} \Omega_p$, and with one material point identified at the centroid of Ω_p. The coordinates of the centroid will be denoted,

$X_p = (R_p, Z_p)$; and the material point initially located at the centroid of each subdomain will be tracked throughout the deformation history of the material. A PIC particle in axisymmetric cylindrical coordinates consists of a ring of material with initial volume obtained by rotating the cross-section Ω_p about the z-axis [6]. The initial mass of a particle in a one radian wedge of volume is

$$m_p = \int_{\Omega_p} \rho_0(X)\, dA_0 \tag{1}$$

where $\rho_0(X)$ is the original mass density of the material and $dA_0 = R\, dR\, dZ$ is an element of area in the original configuration. If ρ_0 is constant then

$$m_p = \rho_p A_p R_p \,, \tag{2}$$

where $\rho_p = \rho_0(R_p, Z_p)$, and A_p is the area of Ω_p.

The density represented by this collection of discrete mass points will be approximated using a Dirac delta function,

$$\rho_0^a(X) = \sum_{p=1}^{N_p} m_p \delta(X - X_p) \,. \tag{3}$$

Using this approximation, the total mass in the region is the same as the total mass given by the continuous density distribution $\rho_0(X)$. Additionally, we have

$$m_p = \int_{\Omega_p} \rho_0(X)\, dA_0 = \int_{\Omega_p} \rho_0^a(X)\, dA_0 \,. \tag{4}$$

Now, consider a transformation to the current configuration in which the same material points that were located at X_p at $t = 0$ are now located at $x_p = (r_p, z_p)$. Conservation of mass can be written

$$\int_{\Omega_2(0)} \rho_0(X)\, dA_0 = \int_{\Omega_2(t)} \rho(x, t)\, dA \,, \tag{5}$$

where $\rho(x, t)$ is the density and dA is an element of area in the current configuration. In deriving an approximation for the density in the current configuration, we require the approximation to satisfy conservation of mass

$$\int_{\Omega_2(0)} \rho_0(X)\, dA_0 = \int_{\Omega_2(t)} \rho^a(x, t)\, dA \,. \tag{6}$$

Let J denote the Jacobian of the transformation from the initial to the current configuration. Using Eqs. (3) and (4), and noting that the Dirac delta function transforms as $\delta(X - X_p) = \delta(x - x_p)/J$ under change of variables, we obtain

$$\int_{\Omega_2(0)} \rho_0(X)\, dA_0 = \int_{\Omega_2(0)} \rho_0^a(X)\, dA_0$$

$$= \int_{\Omega_2(0)} \sum_{p=1}^{N_p} m_p \delta(X - X_p)\, dA_0$$

$$= \int_{\Omega_2(0)} \sum_{p=1}^{N_p} m_p \delta(X - X_p) J\, dA$$

$$= \int_{\Omega_2(t)} \sum_{p=1}^{N_p} m_p \delta(x - x_p) \, \mathrm{d}A \ . \tag{7}$$

Therefore, total mass is conserved if the approximate density in the current configuration is given by

$$\rho^a(x, t) = \sum_{p=1}^{N_p} m_p \delta(x - x_p) \ . \tag{8}$$

Thus, a finite set of material points is identified initially and given a mass m_p consistent with the initial density of the material. The material points keep this same mass throughout the computation, insuring conservation of mass. The material points are also assigned other properties based on the initial conditions for the problem to be solved. For example, each point can be given an initial velocity or initial stress state. The properties assigned initially are updated during the course of a calculation based on the solution of equations of motion on an updated Lagrangian finite element mesh.

2.2. Momentum equation

Let $\rho(x, t)$ be the mass density, $v(x, t)$ be the velocity, $s(x, t)$ be the Cauchy stress tensor, and $b(x, t)$ be the specific body force in the current configuration. The linear momentum equation is given by

$$\rho \frac{\mathrm{d}v}{\mathrm{d}t} = \nabla \cdot s + \rho b \tag{9}$$

Since there are no internal couples, conservation of angular momentum implies that s is symmetric. In the above equation, the time derivative is the material derivative,

$$\frac{\mathrm{d}}{\mathrm{d}t} = \frac{\partial}{\partial t} + v \cdot \nabla \ . \tag{10}$$

The stress is related to the strain through a rate equation which satisfies frame indifference. One such form is the Jaumann rate,

$$\frac{\mathrm{d}s}{\mathrm{d}t} + s \cdot W - W \cdot s = T : \frac{\mathrm{d}e}{\mathrm{d}t} \ , \tag{11}$$

in which T is the fourth-order tangent modulus,

$$\frac{\mathrm{d}e}{\mathrm{d}t} = \frac{1}{2} (\nabla v + \nabla v^{\mathrm{T}}) \tag{12}$$

is the strain rate, and the second-order tensor W is the vorticity tensor,

$$W = \frac{1}{2} (\nabla v - \nabla v^{\mathrm{T}}) \ . \tag{13}$$

For linear elasticity, T is just the constant elasticity tensor, but T is more complicated for elastic-plastic materials. It should be noted that for elastoplasticity T is not formed explicitly in the numerical scheme. Instead, an iterative method is used to solve the constitutive equations [4]. For large deformations, the left side of Eq. (11) is often replaced by the Truesdell, Dienes or some other objective rate. We have chosen the Jaumann rate in Eq. (11) because it is simple to implement numerically and because the shear strains are not large enough in our examples to see the non-physical stress oscillations associated with the Jaumann rate. It is possible to use other rates, in which case Eq. (11) can be thought of as symbolically representing the procedure for solving the constitutive equations.

Eq. (9) is to be solved in time for $x \in \Omega_2(t)$. For a well-posed problem, it is also necessary to augment this equation with appropriate initial conditions, and boundary conditions on the boundary of the domain, $\partial \Omega_2$. Although not completely general, we consider only prescribed displacement or prescribed traction boundary conditions,

$$u(x, t) = g(t) \quad \text{on } \partial \Omega_2^u \ , \tag{14}$$

and

$$s(x, t) \cdot n = t(t) \quad \text{on } \partial \Omega_2^t .$$ (15)

In the above, the boundary is divided into two disjoint sets, $\partial \Omega_2 = \partial \Omega_2^u \cup \partial \Omega_2^t$; n is the unit normal to the boundary; $g(t)$ is the prescribed displacement and $t(t)$ is the prescribed traction. Note that the displacement u is related to the velocity by

$$\frac{du}{dt} = v .$$ (16)

A discretization of the momentum equation is obtained by first writing it in weak form and then choosing a finite-dimensional space in which to seek an approximate solution. The weak form is derived by multiplying Eq. (9) by a test function $w(x, t)$ and then integrating over the domain Ω_3. The test function is assumed to be zero over the part of the boundary where displacement is prescribed. Since all functions, including the test function, are assumed to be independent of θ, integrals over Ω_3 can be reduced to integrals over Ω_2 by integrating out the θ dependence. The result, per radian, is

$$\int_{\Omega_2} \rho w \cdot \frac{dv}{dt} \, dA = \int_{\Omega_2} \rho w \cdot \nabla \cdot s^s \, dA + \int_{\Omega_2} \rho w \cdot b \, dA ,$$ (17)

where $dA = r \, dr \, dz$ is an element of area in Ω_2. The quantity s^s introduced in the last equation is the specific stress, defined by the relation $s = \rho s^s$. Now, integrate the second term in the last equation by parts and apply the divergence theorem to obtain

$$\int_{\Omega_2} \rho w \cdot \frac{dv}{dt} \, dA = - \int_{\Omega_2} \rho \nabla w : s^s \, dA + \int_{\delta \Omega_2^t} w \cdot t \, ds + \int_{\Omega_2} \rho w \cdot b \, dA .$$ (18)

The element of arc length along the boundary is denoted ds.

The computational domain is a region in R^2 containing the material in Ω_2 and it is subdivided into N_e finite elements. For simplicity, the finite element mesh is constructed from 4-node, isoparametric elements. Standard nodal basis functions, $N_i(x)$, associated with the spatial nodes $x_i(t)$, $i = 1, \ldots, N_n$, are assembled from conventional finite element shape functions. Discrete equations are obtained by restricting the velocity, acceleration and test function to be in the span of the nodal basis functions. Therefore, v, dv/dt and w have the following representation

$$v(x, t) = \sum_{i=1}^{N_n} v_i(t) N_i(x) ,$$ (19)

$$\frac{dv}{dt} (x, t) = \sum_{i=1}^{N_n} \frac{dv_i}{dt} (t) N_i(x) ,$$ (20)

and

$$w(x, t) = \sum_{i=1}^{N_n} w_i(t) N_i(x) .$$ (21)

Note that there is no derivative of the shape function in Eq. (20) since equations are solved using isoparametric elements in an updated Lagrangian frame.

Using the representations given in Eqs. (19)–(21) along with the approximation for ρ given in Eq. (8) in the weak form of the momentum equation (18), yields the following discrete weak form

$$\sum_{i=1}^{N_n} w_i(t) \cdot \sum_{j=1}^{N_n} m_{ij}(t) \frac{dv_j}{dt} (t) = - \sum_{i=1}^{N_n} \sum_{p=1}^{N_p} m_p s^s(x_p(t), t) : (w_i(t) \nabla N_i(x))|_{x=x_p}$$

$$+ \sum_{i=1}^{N_n} w_i(t) \cdot \hat{t}_i(t) + \sum_{i=1}^{N_n} w_i(t) \cdot b_i(t) .$$ (22)

New notation has been introduced in Eq. (22). The mass matrix is

$$m_{ij}(t) = \sum_{p=1}^{N_p} m_p N_i(x_p(t)) N_j(x_p(t)) . \tag{23}$$

The discrete applied traction is

$$\hat{t}_i(t) = \int_{\delta\Omega_2^t} N_i(x) t(x, t) \, ds , \tag{24}$$

and the nodal, specific body force is

$$b_i(t) = \sum_{p=1}^{N_p} m_p b(x_p(t), t) N_i(x_p(t)) . \tag{25}$$

To simplify the notation further, the first term on the right-hand side of Eq. (22) can be written in terms of internal forces,

$$-\sum_{i=1}^{N_n} \sum_{p=1}^{N_p} m_p s^s(x_p(t), t) : (w_i(t) \nabla N_i(x))|_{x=x_p} = \sum_{i=1}^{N_n} w_i(t) \cdot f_i^{\text{int}} . \tag{26}$$

Specifically, in axisymmetric cylindrical coordinates, the components of the internal force are $f_i^{\text{int}} = ((f_r)_i^{\text{int}}, (f_z)_i^{\text{int}})$, where

$$(f_r)_i^{\text{int}} = -\sum_{p=1}^{N_p} m_p / \rho_p \left\{ (s_{rr})_p \frac{\partial N_i}{\partial r}(x_p^k) + (s_{rz})_p \frac{\partial N_i}{\partial z}(x_p^k) + (s_{\theta\theta})_p \frac{N_i(x_p^k)}{r_p} \right\} , \tag{27}$$

$$(f_z)_i^{\text{int}} = -\sum_{p=1}^{N_p} m_p / \rho_p \left\{ (s_{rz})_p \frac{\partial N_i}{\partial r}(x_p^k) + (s_{zz})_p \frac{\partial N_i}{\partial z}(x_p^k) \right\} . \tag{28}$$

There are four non-zero components of the stress that contribute to the internal force. The notation for these components evaluated at x_p is $(s_{rr})_p$, $(s_{rz})_p$, $(s_{zz})_p$ and $(s_{\theta\theta})_p$.

The components of w_i are arbitrary except where components of displacement are prescribed. With the understanding that the proper constraints are invoked on the displacement, the discrete form of the momentum equation becomes

$$\sum_{j=1}^{N_n} m_{ij} \frac{dv_j}{dt} = f_i^{\text{int}} + f_i^{\text{ext}} , \tag{29}$$

where the external force vector is

$$f_i^{\text{ext}} = b_i + \hat{t}_i . \tag{30}$$

In practice, the consistent mass matrix is replaced by a diagonal lumped mass matrix whose entries are the corresponding row sum of the consistent mass matrix,

$$m_i(t) = \sum_{p=1}^{N_p} m_p N_i(x_p(t)) . \tag{31}$$

Then, Eq. (31) becomes

$$m_i \frac{dv_i}{dt} = f_i^{\text{int}} + f_i^{\text{ext}} . \tag{32}$$

A consequence of using the lumped mass matrix is that some numerical energy dissipation is introduced, as discussed in [5]. However, the nodal accelerations are no longer coupled so the solution to Eq. (32) is simpler than the solution to Eq. (29).

The discrete equations are to be solved at a discrete set of times, t^k, $k = 1, \ldots, K$. The discrete

approximation at time t^k is indicated by a superscript k, so that m_i^k is the approximation to $m_i(t^k)$, for example. Recall that a new finite element mesh is constructed each timestep; therefore, unlike standard finite element schemes, the data at time t^k for the solution over the time interval $[t^k, t^{k+1}]$ comes from the material points rather than from the spatial mesh. This finite element mesh is also to be used as an updated Lagrangian frame with an explicit time integration. The solution on the nodes of the mesh at the end of the Lagrangian step will be denoted with a superscript L. Thus, in order to solve Eq. (32) for the nodal acceleration, $\mathrm{d}v_i^L / \mathrm{d}t$, the forces at the nodes of the mesh must be defined using Eqs. (27) and (28), and the nodal mass by Eq. (31) at time t^k. Also, in order to use this acceleration in an explicit time integration of the nodal velocity, the velocity at the beginning of the step, v_i^k, must be defined by mapping data from the material points to the nodes. A mass-weighted mapping of the velocity is used for this purpose,

$$m_i^k v_i^k = \sum_{p=1}^{N_p} m_p v_p^k N_i(x_p^k) . \tag{33}$$

Using this value at the beginning of the timestep, the nodal velocity at the end of the Lagrangian step is

$$v_i^L = v_i^k + \Delta t \frac{\mathrm{d}v_i^L}{\mathrm{d}t} . \tag{34}$$

Once the new solution for the nodal acceleration and velocity is obtained from Eqs. (32) and (34), the data at the material points is advanced in time to reflect this solution, as described in the next section.

2.3. Material point equations of motion

New positions of the material points are determined by moving them in the computed velocity field. Eq. (19) defines the velocity field; and the new particle positions are

$$x_p^{k+1} = x_p^k + \Delta t \sum_{i=1}^{N_n} v_i^L N_i(x_p^L) . \tag{35}$$

Note that because we are using isoparametric elements in the updated Lagrangian frame, $N_i(x_p^k) = N_i(x_p^L)$ and it is not necessary to recompute the shape function during the timestep. Furthermore, the velocity field defined by Eq. (19) is single valued so that unphysical material interpenetration is not possible. In a similar fashion, Eq. (20) is used to define the acceleration at the material point position and the velocity is updated according to this acceleration,

$$v_p^{k+1} = v_p^k + \Delta t \sum_{i=1}^{N_n} \frac{\mathrm{d}v_i^L}{\mathrm{d}t} N_i(x_p^L) . \tag{36}$$

The stress and strain are also carried with the material points. A strain increment Δe_p for each material point is computed from the spatial grid,

$$\Delta e_p = \frac{\Delta t}{2} \sum_{i=1}^{N_n} \{ G_{ip}^k v_i^L + (G_{ip}^k v_i^L)^T \} , \tag{37}$$

where

$$G_{ip} v_i = \nabla(v_i N_i(x))|_{x=x_p} \tag{38}$$

is the gradient of the nodal velocity evaluated at x_p. In components, the nodal velocity is written $v_i^L = ((v_r)_p^L, (v_z)_p^L)$, and the strain increments are

$$(\Delta e_{rr})_p = \Delta t \sum_{i=1}^{N_n} (v_r)_i^L \frac{\partial N_i}{\partial r}(x_p^k) ,$$

(39)

$$(\Delta e_{rz})_p = \Delta t \sum_{i=1}^{N_n} \frac{1}{2} \left\{ (v_r)_i^L \frac{\partial N_i}{\partial z}(x_p^k) + (v_z)_i^L \frac{\partial N_i}{\partial r}(x_p^k) \right\} ,$$

(40)

$$(\Delta e_{zz})_p = \Delta t \sum_{i=1}^{N_n} (v_z)_i^L \frac{\partial N_i}{\partial z}(x_p^k) ,$$

(41)

$$(\Delta e_{\theta\theta})_p = \Delta t \sum_{i=1}^{N_n} (v_r)_i^k \frac{N_i(x_p^L)}{r_p} .$$

(42)

The corresponding stress increment, Δs_p, is obtained from the strain increment using standard constitutive equation routines. These routines divide Δe_p into an elastic Δe_p^{el} and plastic Δe_p^{pl} part. The elastic strain increment is then used to update the total elastic strain and the stress for the material point,

$$e_p^{el,k+1} = e_p^{el,k} + \Delta e_p^{el} ,$$

(43)

$$s_p^{k+1} = s_p^k - (s_p^k \cdot W_p^L - W_p^L \cdot s_p^k) + \Delta s_p .$$

(44)

The vorticity is computed from

$$W_p^L = \frac{\Delta t}{2} \sum_{i=1}^{N_n} \{ G_{ip}^k v_i^L - (G_{ip}^k v_i^L)^T \} .$$

(45)

The numerical examples use Von Mises plasticity with an associated flow rule. The yield function, F, has the form

$$F = \bar{s} - H ,$$

(46)

where $\bar{s} = (\frac{3}{2} s^d : s^d)^{1/2}$, s^d is the stress deviator and H is the hardening function. The rate of plastic strain is assumed to follow the evolution equation

$$\frac{\mathrm{d}e^{pl}}{\mathrm{d}t} = \frac{\mathrm{d}\lambda}{\mathrm{d}t} \frac{s^d}{(s^d : s^d)^{1/2}}$$

(47)

in which λ is a monotonically increasing parameter, determined to satisfy the consistency condition, $\mathrm{d}F/\mathrm{d}t = 0$ so that the stress remains on the yield surface, $F = 0$, during plastic flow. The hardening function might depend on equivalent plastic strain,

$$\bar{e}^{pl} = \int \left(\frac{2}{3} \frac{\mathrm{d}e^{pl}}{\mathrm{d}t} : \frac{\mathrm{d}e^{pl}}{\mathrm{d}t} \right)^{1/2} \mathrm{d}t ,$$

(48)

plastic strain rate, or temperature. The numerical solution of the constitutive equations is described in [4]. A nice feature of this method is that when solving the constitutive equations for each material point, the strain history of each point is readily computed for use in history-dependent constitutive equations.

2.4. Energy equation

The energy equation in the continuum for the internal energy per unit mass, e, is written

$$\rho \frac{\mathrm{d}e}{\mathrm{d}t} = s : \frac{\mathrm{d}e}{\mathrm{d}t} ,$$

(49)

if thermal conduction and heat generation are ignored. Since stress and strain are known at the material point locations, the internal energy can be integrated in time at these points. Define e_p^k to be the internal energy per unit mass at x_p^k, then solve

$$\rho_p(e_p^{k+1} - e_p^k) = s^{k+1} : \Delta e_p \tag{50}$$

for e_p^{k+1}. One can add other terms to the discrete energy equation (Eq. (50)) in order to account for the energy dissipation introduced by using the lumped mass matrix and by not using centered time differencing. These terms have been discussed in [1,5], for example, where it is shown that by accounting for this numerical dissipation, the total energy in the discrete system remains constant in time. These issues will not be addressed here since the numerical dissipation is small compared to the energy dissipated due to plastic work. Since the temperature is required in the constitutive equations, it is sufficient for our purposes to compute the temperature T_p^k at x_p^k by assuming that the energy dissipated due to plastic work goes to raise the temperature,

$$\rho_p c_v(T_p^{k+1} - T_p^k) = s_p^{k+1} : \Delta e_p^{pl}, \tag{51}$$

where c_v is the specific heat at constant volume. This approximation is reasonable for the metals considered in the numerical examples.

3. Numerical results

In this section, the solution is presented to three axisymmetric problems, solved in axisymmetric cylindrical coordinates. The first problem is the elastic vibration of a sphere. Since the analytical solution to this problem is known, it provides a simple test that the hoop stress is accounted for correctly in our implementation. It also gives an indication of the numerical dissipation present in the method since theoretically energy should be conserved exactly. The second two problems involve large deformations, one at high speed and one at low speed. The first of these is the Taylor problem of the high speed impact of a cylinder against a rigid surface. The next problem is the quasi-static problem of upsetting of a cylindrical billet. All of these problems were solved on an HP 735 workstation and took between 50 and 60 μs of CPU time per computational cycle, per element.

3.1. Elastic vibrations of a sphere

Fig. 1 shows the representation of the cross-section of a sphere using a collection of material points, superimposed on the computational finite element mesh. The mesh has equal spacing in the r and z directions with $\Delta r = \Delta z = 0.05$ cm, and there are 4 material points per element initially in the part of the domain overlapping the sphere. The sphere has initial radius $R_0 = 0.6$ cm and the computational domain is 1 cm by 2 cm. Notice that the computational finite element domain does not have to conform to the boundary of the sphere; this feature greatly simplifies mesh construction.

The elastic sphere with center at $(0, 1)$ is given an initial radial velocity,

$$v(r, z) = 0.02\sqrt{r^2 + (z - 1)^2}\,\hat{r} \tag{52}$$

which is a good approximation to the velocity corresponding to the fundamental mode of vibration. The exact displacement and velocity corresponding to the fundamental mode have a spatial dependence proportional to the spherical Bessel function of order one, and a sinusoidal time dependence. The frequency of vibration ω is determined by finding the smallest root $x_1 = \omega R_0/c_L$ of the characteristic equation,

$$j_0(x) - \frac{4\mu}{(2\mu + \lambda)x} j_1(x) = 0, \tag{53}$$

where j_0 and j_1 are spherical Bessel functions of order zero and one. The quantities λ and μ are the Lamé constants for the material and c_L is the longitudinal wave speed. For example, copper has
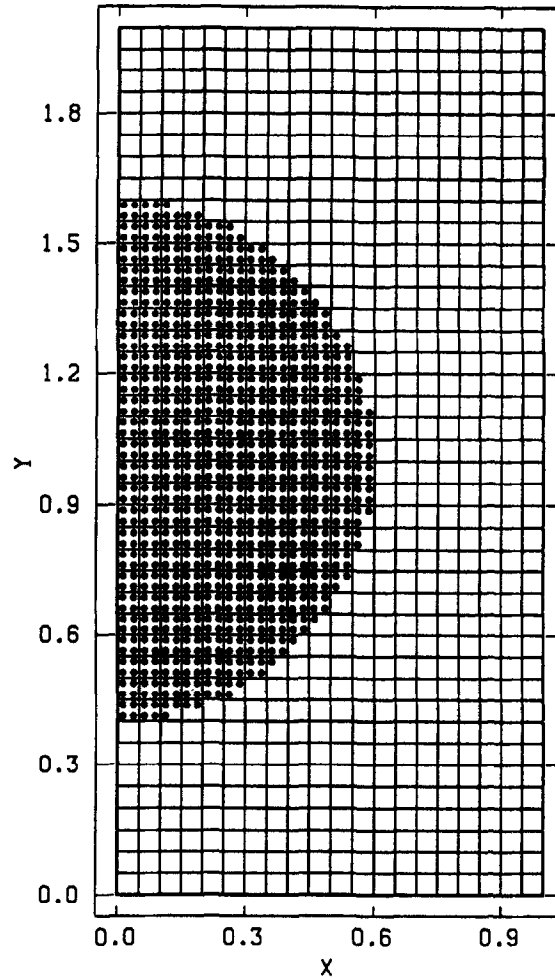
Fig. 1. Material points representing a sphere of radius 0.6 cm are superimposed on a computational mesh. The mesh size is $\Delta r = \Delta z = 0.05$ cm and the computational domain is 1 cm by 2 cm.

$\lambda = 108.6$ GPa, $\mu = 46.6$ GPa, $c_L = 4755$ m/s and the frequency of the fundamental mode for $R_0 = 0.6$ cm is $\omega = 2.204$ MHz.

Elastic vibrations of the copper sphere described above are apparent in a plot of the total kinetic energy of the sphere versus time, as shown in Fig. 2. The computed frequency of vibration ω^c is 2.22 MHz. There is some decay in the kinetic energy over time which is a consequence of numerical dissipation. If it is assumed that the initial amplitude E_0 of the kinetic energy decays exponentially so that it can be represented by a function of the form $E_0 \exp(-\gamma\omega t/2\pi)$, then γ is a measure of the numerical dissipation. Table 1 shows values of the computed frequency and values of γ for varying mesh sizes. As the mesh is refined, γ decreases and ω^c becomes more accurate, as expected.

3.2. Taylor impact

The Taylor problem involves impacting a cylinder at high velocity onto a rigid surface. Using a rigid plasticity model, Taylor [7] determined an approximate relationship between the ratio of the final to initial length of the cylinder and the dynamic yield point of materials. These experiments are still used to test constitutive models and to validate numerical codes [8–11]. Predebon et al. [9] used the Taylor impact test on an aluminum cylinder to validate their method for tracking material history in an Eulerian wavecode. Wilkins and Guinan [8] performed experiments and numerical simulations with
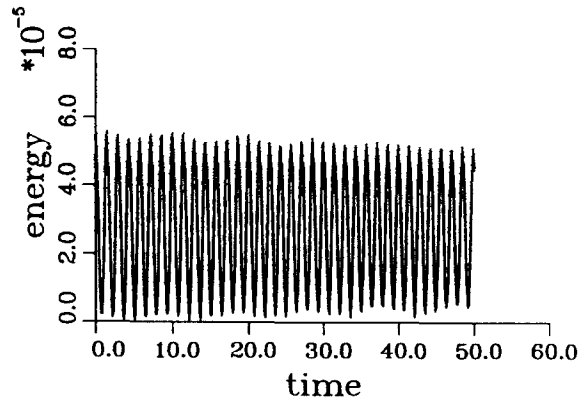
Fig. 2. Kinetic energy $(g\,cm^2/\mu s^2)$ as a function of time (μs) for elastic vibrations of the sphere shown in Fig. 1. The frequency of oscillation and numerical dissipation are measured in Table 1 and compared to similar simulations with varying mesh sizes and time steps.

Table 1
As the mesh is refined, the computed frequency ω^c approaches the theoretical value 2.204 MHz and the energy decay exponent γ goes to zero indicating that numerical dissipation is reduced as the mesh is refined

Convergence with mesh refinement			
Δt (μs)	$\Delta r, \Delta z$ (cm)	ω^c (MHz)	γ
0.16	0.1	2.22	0.0025
0.08	0.05	2.22	0.0060
0.04	0.025	2.20	0.0017

various metals to show a strong correlation between the cylinder length and the yield strength parameter, even when Taylor's rigid-plasticity assumption is dropped. Johnson and Holmquist [10,11] used the Taylor test to compare various constitutive models for OFHC Copper and Armco Iron. Their work involved an experimental component to determine material parameters for various constitutive models, and numerical simulation of the Taylor test to compare the models.

To test our code, a Johnson–Cook constitutive model is used and the results are compared with numerical and experimental results reported in [11]. The Johnson–Cook model includes isotropic hardening, rate effects and thermal softening. The general form for the yield function has a hardening/softening response which is

$$H = (A + B(\bar{e}^{pl})^n)(1 + C\ln(\dot{e}^{pl}))(1 - T^{*m}).$$ (54)

Table 2
Parameters used in the simulation of the Taylor impact problem

Material parameters for OFHC copper	
Density	8940 kg/m³
Young's modulus	115 GPa
Poisson's ratio	0.31
Melting temperature	1083°C
Specific heat	385 J/kg °C
Parameters for Johnson–Cook model	
A	65 MPa
B	356 MPa
C	0.013
n	0.37
m	1.05

The quantity $\dot{e}^{\text{Pl}}$ is a dimensionless strain rate, scaled by the nominal value $1\,\text{s}^{-1}$; and T^* is the homologous temperature. The model contains five parameters, A, B, C, n and m. Values of these parameters determined from tension tests for OHFC copper are reported in [11] and are repeated in Table 2 along with other material properties of OFHC copper used in the numerical simulations.

Fig. 3(a) shows the initial geometry of the cylinder and 15×37 computational mesh. The initial height of the cylinder is $L_0 = 25.4\,\text{mm}$ and the initial diameter is $D_0 = 3.8\,\text{mm}$. The mesh spacing is $\Delta r = \Delta z = 0.76\,\text{mm}$, with 4 material points per element. After 50 μs with an initial vertical velocity of $190\,\text{m/s}$, the deformation is quite severe, as shown in Fig. 3(b). The predicted final length, diameter and bulge are $L_f = 18.3\,\text{mm}$, $D_f = 14.6\,\text{mm}$ and $W_f = 9.12\,\text{mm}$, respectively. The final diameter is measured at the impact surface and the bulge is the diameter of the cylinder measured at $0.2L_0$ up from the impact surface. Compared to an experimental test [11] the final diameter and length are somewhat larger and the bulge is smaller. Johnson and Holmquist [10] introduce an error measure defined as follows:

$$\bar{\Delta} = \frac{1}{3}\left[\frac{|\Delta L|}{L_T} + \frac{|\Delta D|}{D_T} + \frac{|\Delta W|}{W_T}\right], \tag{55}$$

where $\Delta L = L_f - L_0$, $\Delta D = D_f - D_0$, $\Delta W = W_f - W_0$, and L_T, D_T, W_T are the length, diameter and bulge
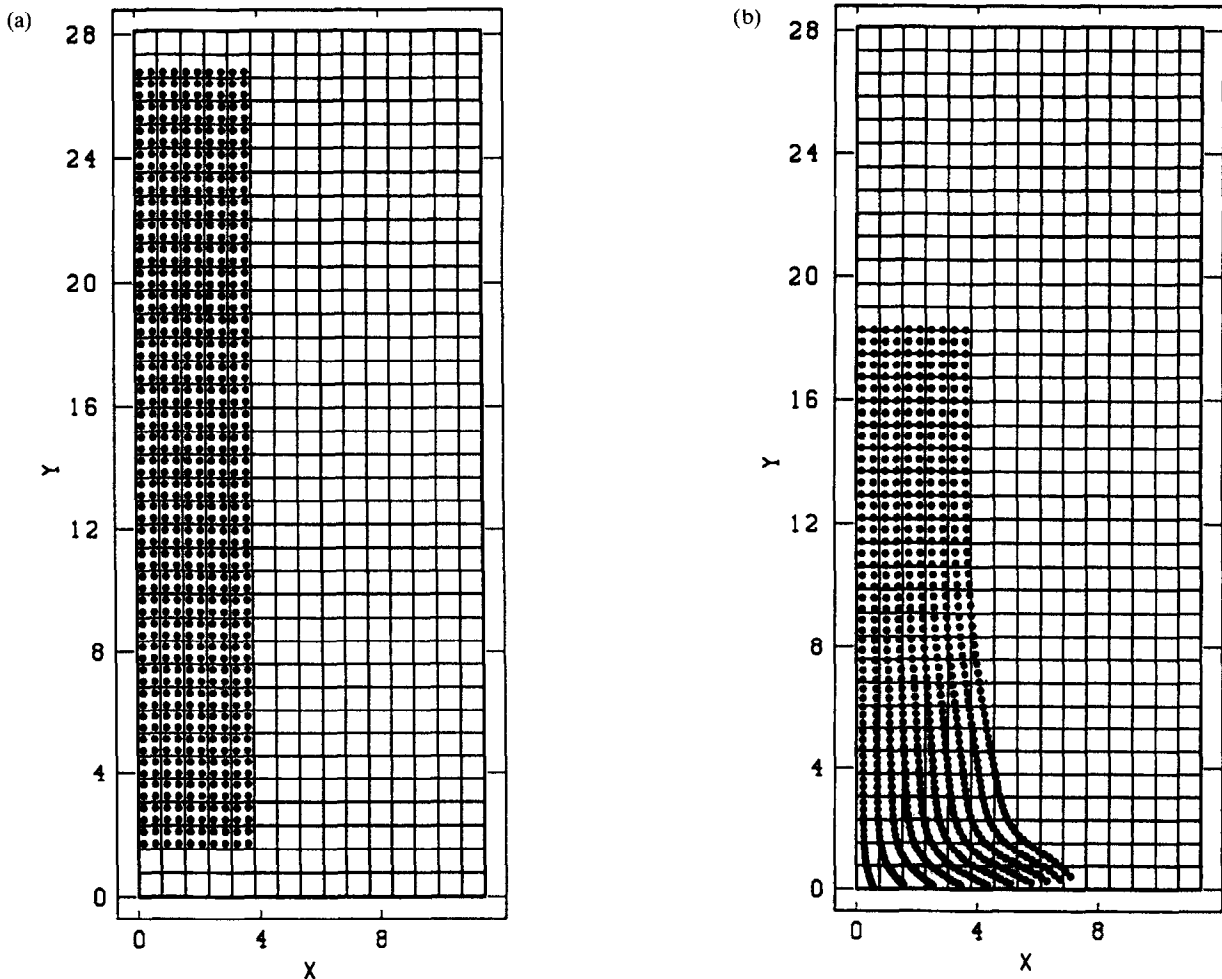

Fig. 3. (a) The initial configuration of material points and computational mesh for an elasto-plastic copper cylinder given an initial downward velocity of $0.190\,\text{mm/μs}$. The cylinder is $25.4\,\text{mm}$ in length and $3.8\,\text{mm}$ in radius and the mesh size is $\Delta r = \Delta z = 0.76\,\text{mm}$. (b) The final deformation of the cylinder described in (a) after 50 μs. The computed cylinder profile is compared with experimental results in Table 3.

Table 3

Comparison between experimental [11] and computed values of diameter, bulge and length for the impact of a copper cylinder against a rigid surface. The diameter is measured at the impact surface and the bulge is the diameter measured $0.2L_0 = 5.08$ mm up from the impact surface

Results of Taylor impact study

	Initial geometry	Final geometry (experimental)	Final geometry (numerical)
Diameter	3.8 mm	13.5 mm	14.6 mm
Bulge	3.8 mm	10.1 mm	9.12 mm
Length	25.4 mm	16.2 mm	18.3 mm

measured in an experimental test. Our results give $\bar{\Delta} = 0.10$ whereas Holmquist and Johnson [11] report $\bar{\Delta} = 0.04$ for a calculation using the EPIC code. The test data and final data are given in Table 3. These calculations were repeated with a 30×74 mesh and a 60×148 mesh and there was no measurable change in the cylinder profile.

Contours of the equivalent plastic strain at 50 μs are shown in Fig. 4(a) for the copper cylinder. These predictions agree well with the EPIC computations reported in [11]. Fig. 4(b) is a plot showing contours of the temperature increase (above room temperature, 20°C), and Fig. 4(c) shows contours of
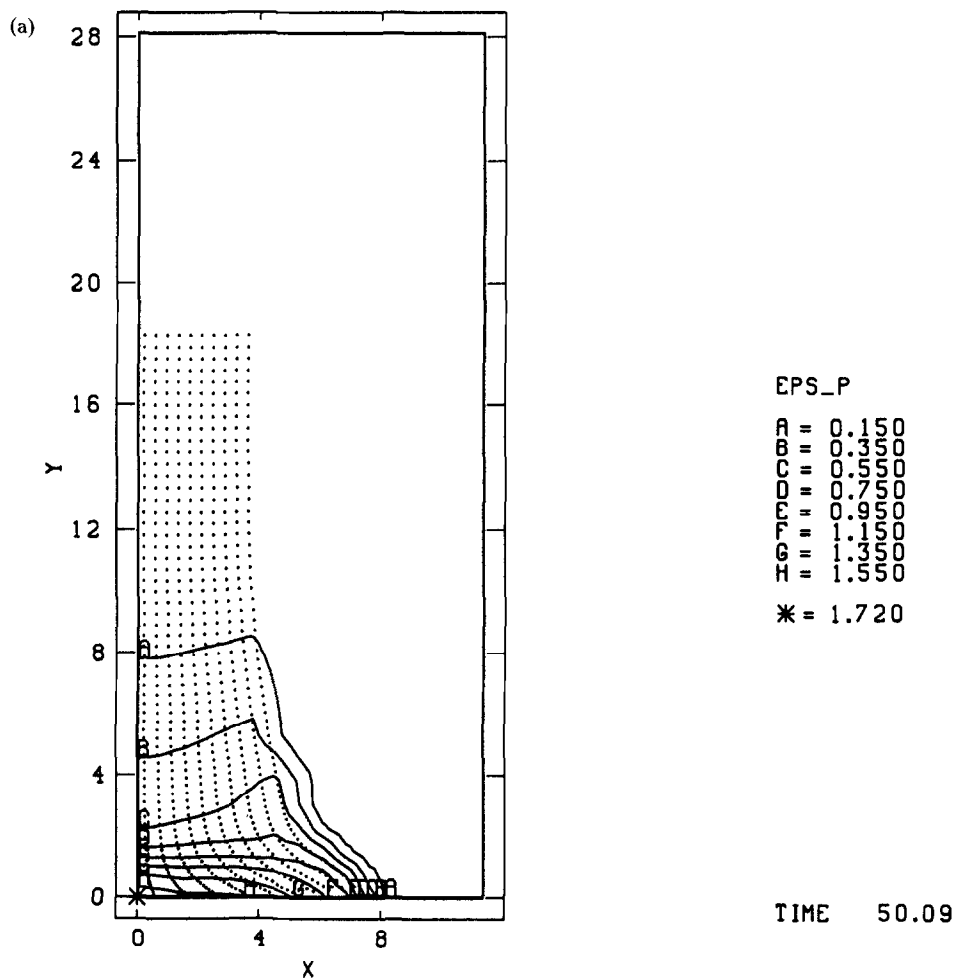

Fig. 4. Contours of (a) plastic strain, (b) temperature increase (°C) and (c) Mises equivalent stress (g/mm μs²) after impact of the copper cylinder shown in Fig. 3.
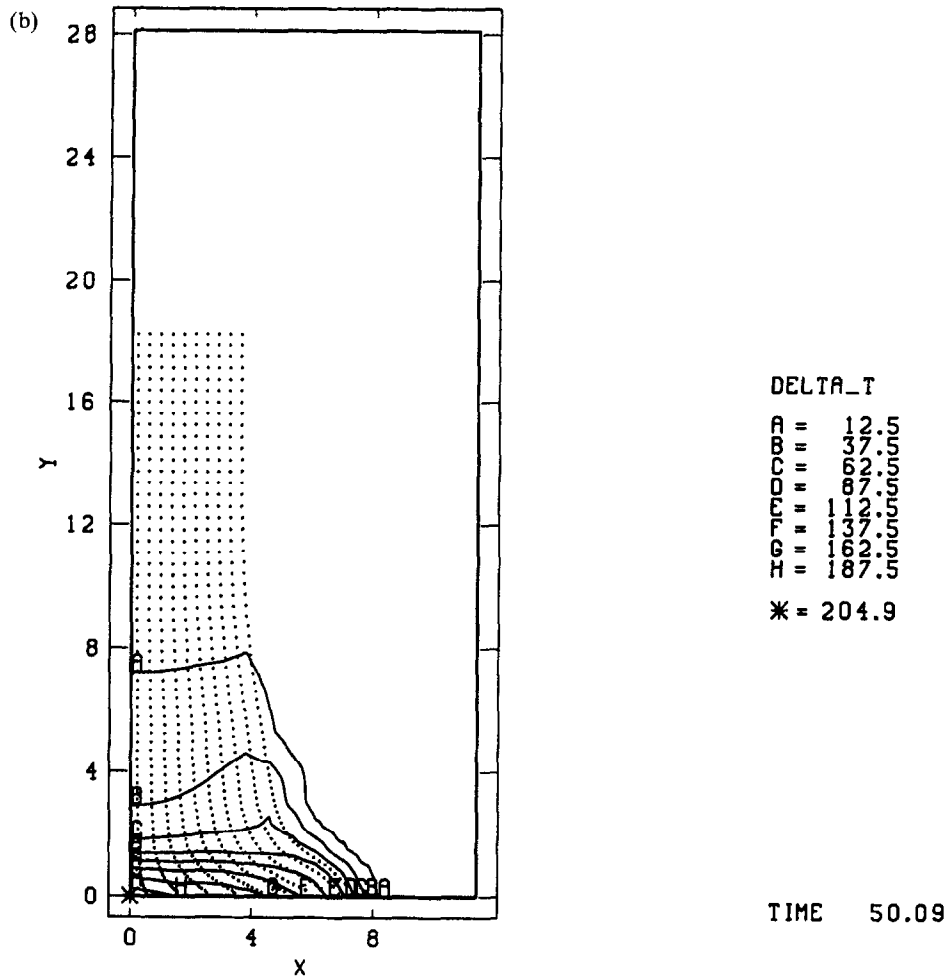
Fig. 4. (Contd.)

equivalent stress. These results are consistent with the assumption that the temperature rise is due to heat generated by plastic work. The maximum temperature increase approximately equals the maximum equivalent plastic strain times the equivalent stress divided by the density and specific heat. The plastic strain, temperature and equivalent stress increase slightly with mesh refinement. The maximum values on the finest mesh are 2.01, 250°C, and 562 MPa. Numerically, we find thermal softening and the rate effects in the constitutive model have little effect on the final deformation of the cylinder.

3.3. Upsetting of a cylindrical billet

In upsetting, a cylindrical billet is compressed between two platens. This process is used in manufacturing as a means to pre-form workpieces prior to applying another operation such as rolling or extrusion. This problem was proposed as a benchmark for numerical codes in [12] and 14 researchers reported results obtained by their method of choice. Five of these computations used an elastic-plastic formulation with the same constitutive equation and the others used a rigid-plastic simulation method. In order to eliminate ambiguities related to implementation of a friction algorithm, these simulations were carried out assuming that the platens were rough. The element type, number of elements and deformation increment were all left to the individual investigator. The goal was to simulate 60% upsetting and some of the investigators were not able to run their codes to completion. The predicted behavior also varied considerably among the investigations.
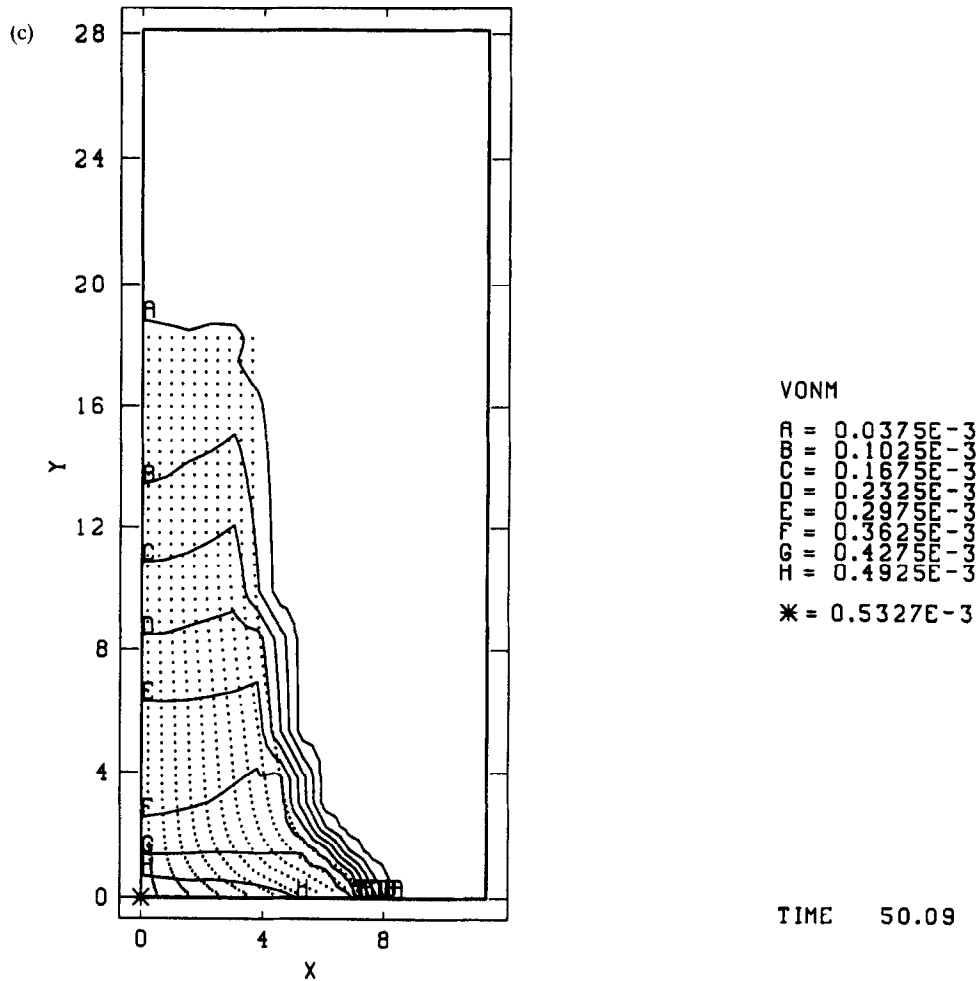
Fig. 4. (Contd.)

The benchmark problem consists of a steel cylinder 20 mm in diameter and 30 mm in height. The left side of Fig. 5 shows the representation of this cylinder using material points. Only half the cylinder is modeled due to the symmetry about the midline, $z = 0$. The platen, also shown in Fig. 5, is modeled with material points that move as a rigid body. The platen starts above the workpiece and moves down at a constant velocity of 1 m/s, compressing the billet. There is no slip allowed between the platen and the cylindrical workpiece. The steel has a Young's modulus of 200 GPa, Poisson's ratio of 0.3, density of 7800 kg/m³, and an initial yield strength of 0.70 GPa with a strain hardening slope of 0.30 GPa; i.e. the hardening function is

$$H = 0.70 + 0.30\bar{e}^{\text{pl}}\ \text{GPa} .\tag{56}$$

The final configuration of material points is shown on the right side of Fig. 5 after 60% upsetting (i.e. reduction to 40% of the original height). This figure is the result of using a 24 × 18 mesh where $\Delta r = \Delta z = 1$ mm. The same simulation was run on 48 × 36 and 96 × 72 meshes with no change in the final cylinder profile.

Fig. 6(a–c) gives the load–displacement curve predicted by the simulations on three different meshes. These are oscillations present in these curves. The larger jumps are probably due to material folding against the platen, as noted in [13]. The smaller amplitude oscillations are most likely the result of our explicit time integration scheme and a fairly crude contact algorithm for the contact between the rigid lid and the deformable body. An implicit time integration scheme would be useful for quasi-static
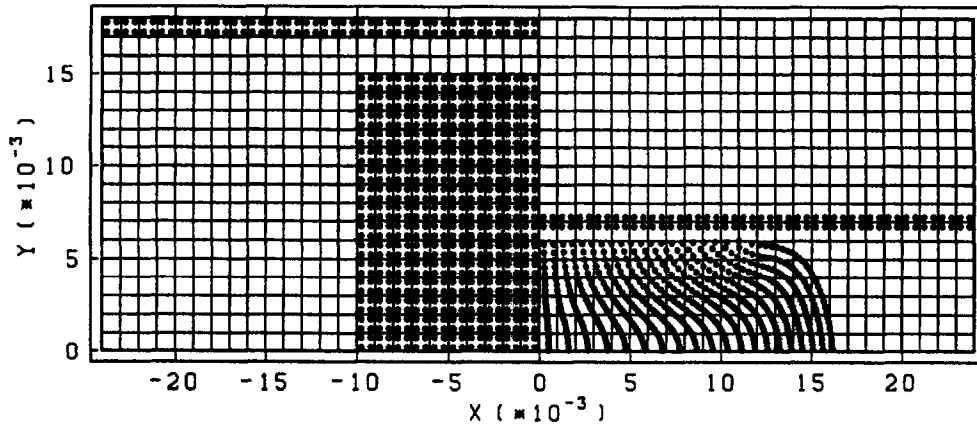
Fig. 5. On the left, the initial configuration of material points superimposed on the computational grid for a cylinder of length 0.03 m and radius 0.01 m. Only half the cylinder is modeled. On the right, the configuration of the cylinder after 60% upsetting. The mesh contains 24 × 18 square elements, 1 mm on a side, with 4 material points per element.
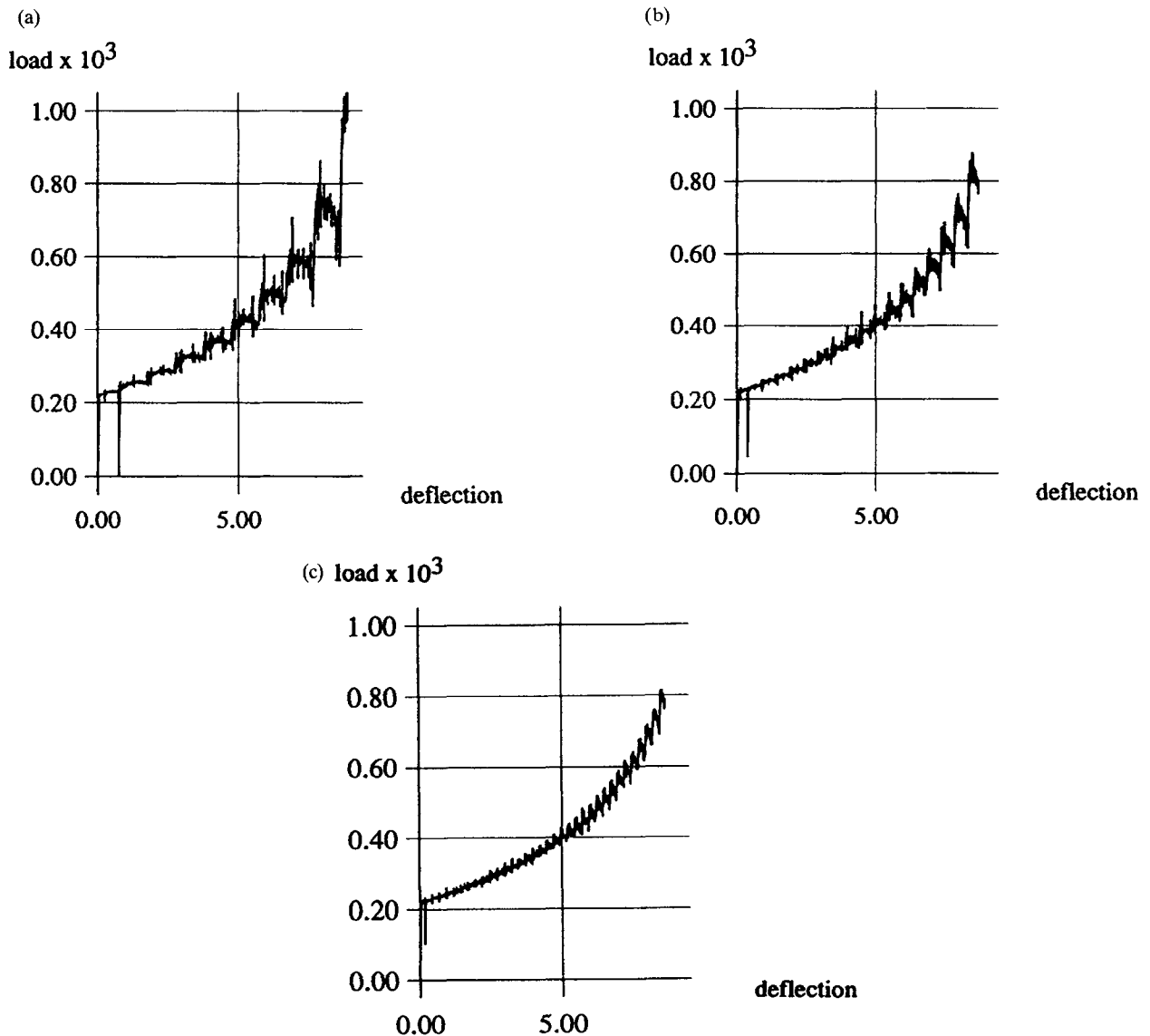
(a)

load x 10^3

(b)

load x 10^3

(c) **load x 10^3**

Fig. 6. Load (kN) versus deflection (mm) curve for the 60% upset problem on a (a) 24 × 18; (b) 48 × 36; (c) 96 × 72 mesh.
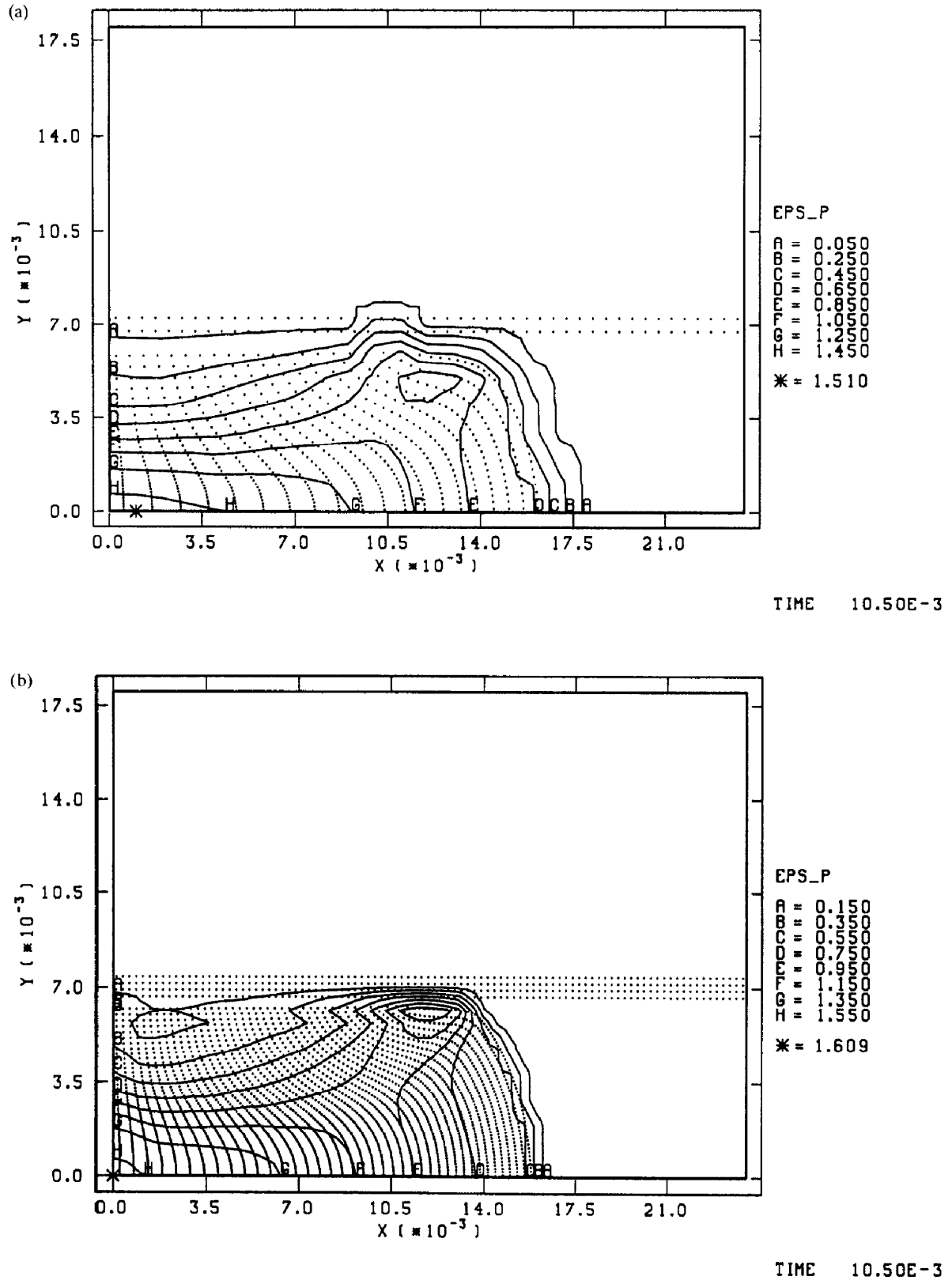
Fig. 7. Contours of plastic strain at 60% upset for the cylinder (a) on a 24 × 18 mesh shown in Fig. 5; (b) a 48 × 36 mesh; (c) a 96 × 72 mesh. A localized region of high strain where material folds against the platen becomes more apparent as the mesh is refined.
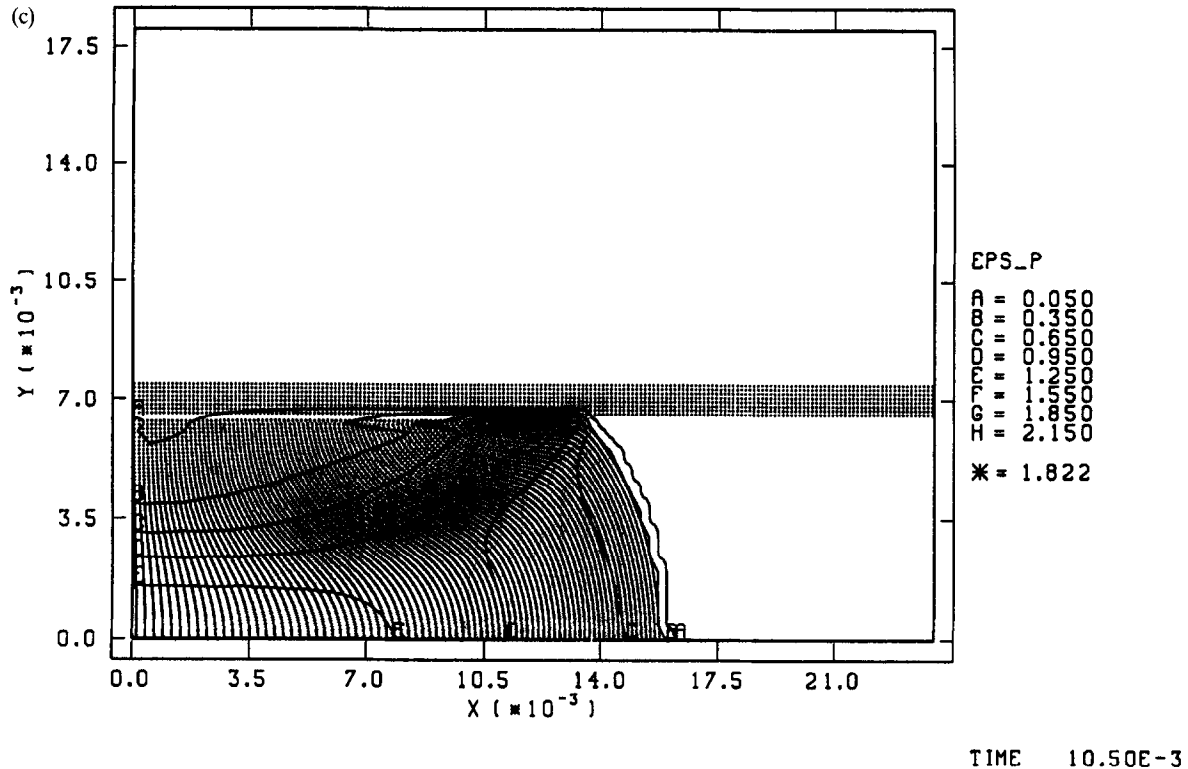
Fig. 7. (Contd.)

calculations, such as this one, and is planned for the future. The contact algorithm will also be examined in future studies. The load at maximum deflection is reduced somewhat for the finer mesh, but does not change appreciably with mesh refinement, except that the magnitude of the oscillations continues to reduce. The predicted maximum load is about 800 kN.

Fig. 7(a–c) shows contours of plastic strain for different mesh resolutions. Mises equivalent stress and temperature rise as predicted by the material point code are shown in Fig. 8(a–b) for the coarse resolution (24 × 18) mesh. Regions of large plastic strain and temperature rise occur in the center of the billet (along the midline, $z = 0$). There is also a local region of high strain and temperature where the billet folds against the platen. Mesh refinement indicates that the high-strain region near the platen might be an area where localized damage would occur, if permitted by the constitutive equation. The plastic strain in Fig. 7(a–c) increases with mesh refinement in the region where folding occurs. It continues to rise in this region, and becomes more localized, as the mesh is refined; however it does not change near the midline of the cylinder on the finer meshes. The same pattern is seen with equivalent stress and temperature rise (not shown), indicating that there might be a singularity in the flow where the folding occurs.

Some of the difficulties associated with this problem are severe distortion and folding of material against the platens as upsetting progresses. It is difficult for 4 node, bilinear, quadrilateral elements in an updated Lagrangian frame to model the folding since two adjacent edges become coincident when the material folds against the platens [14]. In recent work, the same problem was solved by Taylor and Becker [14], Shih and Yang [13] and Tuğcu [15]. Since the latter work uses a slightly different constitutive model, we compare our results to the first two. These simulations use a 6 × 9 cross-triangular mesh of elements and an 8 × 12 mesh of 4 node quadrilateral elements with 8 degrees of freedom, respectively. Our coarse mesh calculation uses 8 × 10 elements to represent the cylinder initially and therefore has about the same resolution. Figs. 5, 6(a), 7(a) and 8(a,b) show that results from the material point code for the coarse mesh agree with the results in [14] and [13] although there are some differences in detail. (There are also differences in detail between the results in [14] and [13].)
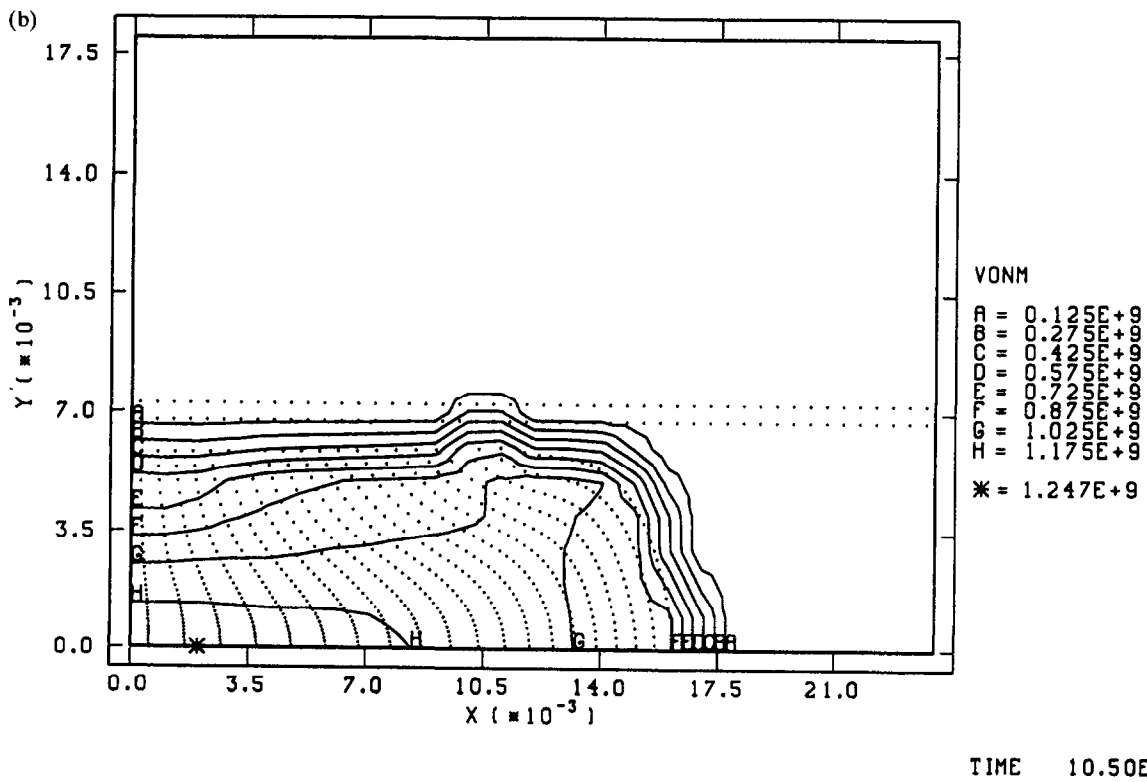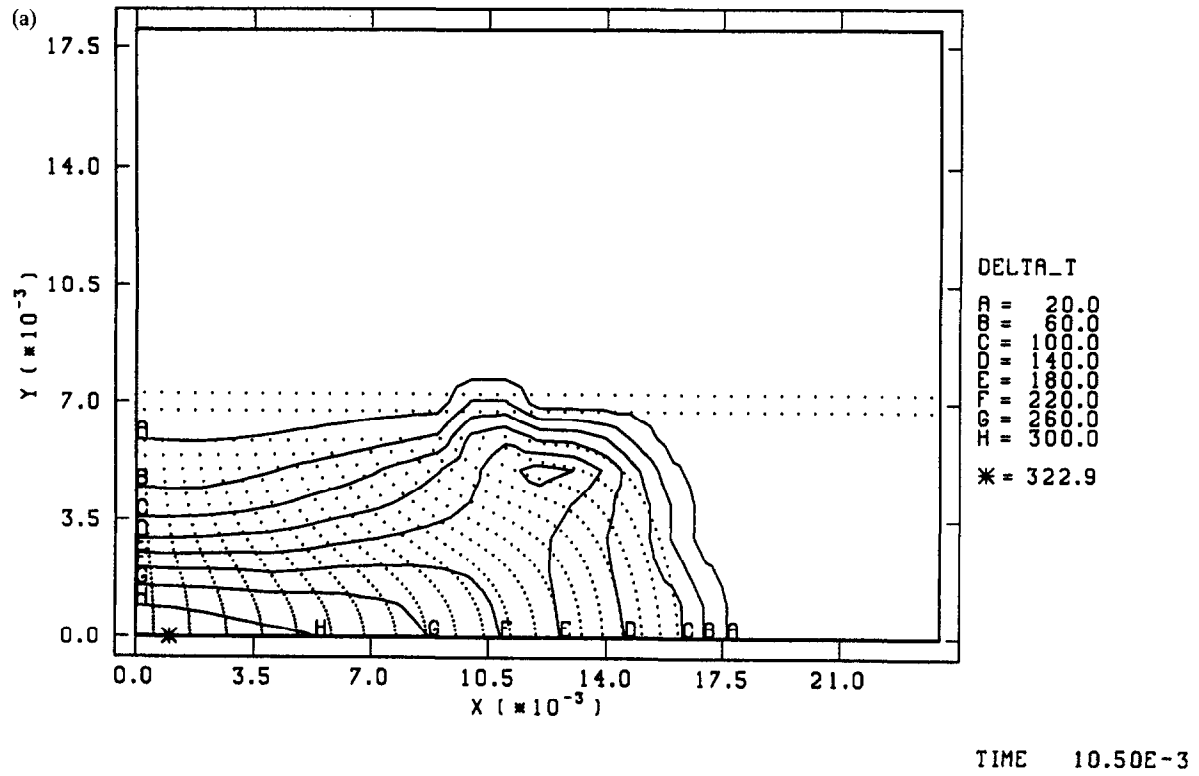
Fig. 8. Contours of (a) temperature increase (°C) and (b) Mises equivalent stress (Pa) at 60% upset for a simulation using a 24 × 18 mesh.

Simo et al. [16], also consider an upsetting problem in order to assess the performance of their enhanced strain elements compared to other elements. Their study is three-dimensional and apparently uses a friction-free interface condition on the platen surface and a slightly different constitutive equation than the benchmark problem. Nevertheless, their conclusions about the performance of various element types should hold for the present situation. In particular, under-integration can produce pathological results in some cases, and the standard tri-linear brick element produces an unsatisfactorily stiff response. This is not in evidence for the material point calculation even though the background finite element mesh is based on standard bilinear quadrilateral elements. The load–deflection curves in Figs. 6(a–c) give no indication of an overly stiff response. A possible reason for the behavior of the material point method is that elements only have to represent a (usually small) deformation increment, rather than the total deformation. Each step in our calculations is begun from a uniform mesh.

4. Conclusion

A general description of the material point code has been presented, along with special considerations relevant to axisymmetric problems. The method utilizes a material or Lagrangian mesh defined on the body under investigation, and a spatial or Eulerian mesh defined over the computational domain. The set of material points making up the material mesh is tracked throughout the deformation history of the body and these points carry with them a representation of the solution in a Lagrangian frame. Interactions among these material points are computed by projecting information they carry onto a background finite element mesh where equations of motion are solved. The solution to these equations is then used to update the material points.

The material point method provides a framework for studying large strain problems and can include effects of elasticity, viscoplasticity and temperature. The mesh construction is particularly simple; the algorithm is efficient enough so that analyses can be performed on workstations; and the results show convergence with mesh refinement and only a small amount of numerical dissipation. Even though the background finite element mesh is constructed out of standard four node quadrilateral elements, the material point method does not exhibit locking or an overly stiff response in simulations of upsetting. Mesh tangling is also not an issue in large deformation simulations. The results reported here for upsetting and Taylor impact problems agree well with predictions by other numerical solution techniques and with experiments. The sample problems also illustrate the capability to solve high speed impact problems as well as low speed manufacturing problems.

References

[1] J.U. Brackbill and H.M. Ruppel, FLIP: A method for adaptively zones, particle-in-cell calculations in two dimensions, J. Comput. Phys. 65 (1986) 314–343.

[2] J.U. Brackbill, D.B. Kothe and H.M. Ruppel, FLIP: A low-dissipation, particle-in-cell method for fluid flow, Comput. Phys. Comm. 48 (1988) 25–38.

[3] D. Sulsky, Z. Chen and H.L. Schreyer, A particle method for history-dependent materials, Comput. Methods Appl. Mech. Engrg. 118 (1994) 179–196.

[4] D. Sulsky, S.-J. Zhou and H.L. Schreyer, Application of a particle-in-cell method to solid mechanics, Comput. Phys. Comm. 87 (1995) 236–252.

[5] D. Burgess, D. Sulsky and J.U. Brackbill, Mass matrix formulation of the FLIP particle-in-cell method, J. Comput. Phys. 103 (1992) 1–15.

[6] J.M. Wallace, J.U. Brackbill and D.W. Forslund, An implicit moment electromagnetic plasma simulation in cylindrical coordinates, J. Comput. Phys. 63 (1986) 434–457.

[7] G.I. Taylor, The use of flat-ended projectiles for determining dynamic yield stress. Part I, Proc. R. Soc. London, Ser. A 194 (1948) 289–299.

[8] M.L. Wilkins and M.W. Guinan, Impact of cylinders on a rigid boundary, J. Appl. Phys. 44 (1973) 1200–1206.

[9] W.W. Predebon, C.E. Anderson and J.D. Walker, Inclusion of evolutionary damage measures in Eulerian wavecodes, Comput. Mech. 7 (1991) 221–236.

[10] G.R. Johnson and T.J. Holmquist, Evaluation of cylinder-impact test data for constitutive model constants, J. Appl. Phys. 64 (1988) 3901–3910.

[11] T.J. Holmquist and G.R. Johnson, Determination of constants and comparison of results for various constitutive models, Journal De Physique IV, Colloque C3, suppl. au Journal de Physique III 1 (1991) C3-853–C3-860.

[12] H. Kudo and S. Matsubara, Joint examination project of validity of various numerical methods for the analysis of metal forming processes, in: H. Lippmann, ed., Metal Forming Plasticity (Springer-Verlag, Berlin, 1979).

[13] A.J.M. Shih and H.T.Y. Yang, Experimental and finite element simulation methods for rate-dependent metal forming processes, Int. J. Numer. Methods Engrg. 31 (1991) 345–367.

[14] L.M. Taylor and E.B. Becker, Some computational aspects of large deformation, rate-dependent plasticity problems, Comput. Methods Appl. Mech. Engrg. 41 (1983) 251–277.

[15] P. Tuğcu, Thermomechanical analysis of upsetting of a cylindrical billet, Comput. Struct. 58 (1996) 1–12.

[16] J.C. Simo, F. Armero and R.L. Taylor, Improved versions of assumed enhanced strain tri-linear elements for 3D finite deformation problems, Comput. Methods Appl. Mech. Engrg. 110 (1993) 359–386.